Chinese Chemical Letters 37 (2026) 112794

Contents lists available at ScienceDirect

Chinese Chemical Letters

journal homepage: www.elsevier.com/locate/cclet

Predictive interstitial boron doping in 3D cross-linked ultrathin Nb_2O_5 *via* atomic-mismatch engineering for enhanced catalytic performance

Minghui Chen[a], Lei An[a], Kaiwei Wang[a], Jianing Qian[a], Yuming Chen[a], Xingtao Xu[b,c,*], Tianjun Ni[a,d,*], Dong Liu[a,*]

[a] School of Public Health, Henan Medical University, Xinxiang 453003, China
[b] Department of Materials Process Engineering, Graduate School of Engineering, Nagoya University, Nagoya 464-8603, Japan
[c] Marine Science and Technology College, Zhejiang Ocean University, Zhoushan 316022, China
[d] School of Basic Medical Sciences, Henan Medical University, Xinxiang 453003, China

ARTICLE INFO

Article history:
Received 4 January 2026
Revised 7 April 2026
Accepted 16 April 2026
Available online 17 April 2026

Keywords:
Niobium pentoxide
Interstitial doping
Atomic mismatch
Doxorubicin degradation
Toxicity analysis

ABSTRACT

Niobium pentoxide (Nb_2O_5) is a promising yet inefficient photocatalyst due to its wide bandgap, rapid charge recombination, and limited active sites. Herein, we propose a predictive doping paradigm guided by multi-dimensional atomic mismatch (in ionic radius, valence state, and element nature) to direct boron into interstitial sites within a three-dimensional (3D) cross-linked ultrathin Nb_2O_5 architecture. This atomic-mismatch-guided interstitial doping effectively engineers the electronic structure, substantially reducing the exciton binding energy and creating long-lived shallow traps for charge carriers. The deliberately constructed 3D porous network provides abundant exposed active sites, high adsorption capacity, and enhanced mass transport. Synergistically, the tailored electronic structure enables highly efficient visible-light photocatalysis. In the optimized catalyst (BNO-2), this synergistic mechanism leads to exceptional doxorubicin (DOX) degradation (96.9 % within 30 min) under visible light, along with effective detoxification and progressive mineralization. Mechanistic studies identify the superoxide radical as the predominant reactive species. This work not only establishes a novel predictive doping paradigm based on atomic mismatch but also demonstrates the capability of concurrently engineering nanoarchitecture and electronic structure to design high-performance environmental remediation materials.

© 2026 Published by Elsevier B.V. on behalf of Chinese Chemical Society and Institute of Materia Medica, Chinese Academy of Medical Sciences.

The escalating prevalence of persistent pharmaceutical contaminants in global water resources represents a critical environmental challenge, jeopardizing ecosystem stability and public health [1,2]. Among these emerging micropollutants, anticancer drugs are of particular concern owing to their designed bioactivity and potential to induce cytotoxic, mutagenic, and carcinogenic effects even at minimal concentrations [3,4]. Doxorubicin (DOX), a widely used anthracycline antibiotic, epitomizes this threat [5]. Its pronounced chemical stability and low biodegradability contribute to environmental persistence, with detectable levels reported in wastewater effluents, underscoring the urgent need for advanced remediation strategies [6–10]. This urgency calls for the development of efficient and sustainable technologies capable of not only decomposing but also detoxifying such persistent pharmaceutical threats through catalysts with high density of accessible active sites.

Semiconductor photocatalysis, as a sustainable advanced oxidation process, holds significant potential for the destructive removal of such recalcitrant organic compounds [11,12]. Nevertheless, its efficiency is intrinsically dictated by the physicochemical properties of the photocatalyst [13,14]. Niobium pentoxide (Nb_2O_5) has garnered considerable attention as a promising photocatalytic material due to its non-toxicity, robust chemical stability, and potent oxidative capacity [15–18]. While TiO_2 and ZnO are among the most widely studied metal oxide photocatalysts, Nb_2O_5 presents distinct advantages for this specific doping strategy and application. Its relatively flexible and open crystal structure, compared to the denser lattices of TiO_2 and ZnO, provides more accessible interstitial sites, which is crucial for realizing our atomic-mismatch-guided interstitial doping paradigm. Nb_2O_5 exhibits superior chemical and photochemical stability, especially in aqueous environments, preventing photocorrosion, a common issue for ZnO under prolonged illumination. In addition, its intrinsic strong oxidative capacity (more positive valence band potential than TiO_2) is highly suitable for generating potent oxidizing species to degrade recalcitrant pharmaceuticals like doxorubicin. Finally, the acidic surface properties

* Corresponding authors.
E-mail addresses: xingtao.xu@zjou.edu.cn (X. Xu), tjni@xxmu.edu.cn (T. Ni), liudong081@163.com (D. Liu).

https://doi.org/10.1016/j.cclet.2026.112794
1001-8417/© 2026 Published by Elsevier B.V. on behalf of Chinese Chemical Society and Institute of Materia Medica, Chinese Academy of Medical Sciences.

of Nb_2O_5 can be advantageous for the adsorption of basic organic pollutants, providing a synergistic platform for the intended "adsorption-photocatalysis" mechanism. Therefore, Nb_2O_5 serves as an ideal host matrix to validate our predictive doping concept and construct a robust, synergistic system for advanced water remediation. However, the practical deployment of pristine Nb_2O_5 is hampered by inherent shortcomings: A wide bandgap (~3.4 eV) that limits light absorption to the ultraviolet region, rapid recombination of photogenerated electron-hole pairs, and a relatively low specific surface area with insufficient exposed active sites, which restricts reactant adsorption and interfacial catalytic reactions [18–24]. These intrinsic electronic and architectural limitations severely restrict its practical application and motivate the exploration of effective strategies to engineer its band structure and charge carrier dynamics, and surface architecture to maximize active site exposure.

To address these constraints, elemental doping has been extensively adopted as a viable approach to modulate the electronic properties of semiconductors [22,25–28]. In this work, we establish a predictive doping paradigm guided by multi-dimensional atomic mismatch. Conventional doping strategies often prioritize substitutional doping, wherein dopant atoms replace host cations of comparable size and valence [29,30]. In contrast, our strategy is designed to exploit the pronounced mismatch in ionic radius, valence state, and element nature (nonmetallic B^{3+} *vs.* metallic Nb^{5+}) [31–33]. This deliberate mismatch establishes a thermodynamic driving force that preferentially promotes dopant occupation of interstitial sites. This pathway is preliminarily validated by our earlier work on iodine-doping [34], and the resulting electronic modulations are distinct from and potentially superior to those arising from substitutional doping [19,35–40]. This understanding unveils new opportunities for tailoring material properties, particularly in low-dimensional nanostructures. In ultrathin materials, substitutional doping can introduce localized strain or disrupt crystalline integrity [41]. Interstitial doping, by occupying sites between lattice layers, minimizes structural disruption while effectively modulating electron density, introducing active sites, and facilitating charge transfer pathways [25]. Thus, it preserves the inherent benefits of the nanoscale morphology while conferring additional functionality.

Given the predictive value of the mismatch-guided paradigm, we test its generality by applying it to boron (B). Boric acid (H_3BO_3, B^{3+}) is selected as an ideal model dopant precisely because it exhibits a pronounced multi-dimensional mismatch with Nb^{5+}: A much smaller ionic radius, a lower valence state, and a distinct nonmetallic nature. In terms of ionic radius, B^{3+} measures approximately 0.27 Å (coordination number 4) or 0.41 Å (coordination number 6), whereas Nb^{5+} is about 0.64 Å (coordination number 6). The ionic radius of B^{3+} is significantly smaller than that of Nb^{5+} (by about 40 %−60 %), which makes it difficult for B^{3+} to substitute for Nb^{5+} in the lattice and instead favors its occupation of interstitial sites. Regarding valence state, B possesses a +3 oxidation state, while Nb exhibits a +5 oxidation state. The lower valence of B^{3+} relative to Nb^{5+} leads to charge mismatch, and doping is expected to introduce local charge–compensation mechanisms that alter the electronic structure. With respect to elemental nature, B is a non–metal with an electronegativity of 2.04, whereas Nb is a transition metal with an electronegativity of 1.6. Their pronounced differences in electronegativity and chemical–bonding characteristics further enhance the potential for electronic–structure modulation. According to our paradigm, these intrinsic disparities are predicted to unequivocally drive boron into interstitial sites within the Nb_2O_5 lattice [42,43]. H_3BO_3 undergoes low-temperature decomposition (around 400 °C) to yield highly reactive B_2O_3 or B-O species. This moderate thermal decomposition allows boron atoms to diffuse dynamically and controllably into the interstitial sites of the Nb_2O_5 lattice during calcination, avoiding phase separation or structural collapse that could result from aggressive reactions, which is crucial for achieving homogeneous interstitial doping. Moreover, H_3BO_3 releases water vapor during its thermal decomposition process. The released gas can etch and expand the pores in the formed Nb_2O_5, thereby significantly increasing the specific surface area and porosity of the material. This is consistent with our goal of constructing a 3D cross-linked porous superstructure. Notably, B is a nonmetallic element with high electronegativity, fundamentally distinct from the metallic nature of Nb. This intrinsic difference in element category, combined with the pronounced ionic-radius and valence-state mismatch, further reinforces the thermodynamic driving force for interstitial incorporation over conventional substitutional doping. We posit that this pronounced atomic mismatch will unequivocally direct boron into interstitial sites within the Nb_2O_5 lattice. More critically, we propose that these interstitial B species, being small and highly electron-deficient, will function as potent electronic modulators. They are anticipated to exert a strong perturbation on the Nb-O framework, achieving targeted electronic structure engineering by generating mid-gap states, narrowing the bandgap, and acting as efficient traps for charge carriers [44]. Furthermore, we hypothesize that coupling this atomic-mismatch-guided interstitial boron doping with a three-dimensional hierarchical architecture constructed from ultrathin Nb_2O_5 nanosheets will yield a synergistic enhancement in photocatalytic performance. The 3D porous superstructure mitigates nanosheet restacking, promoting mass transport and light penetration [45,46], and creating abundant accessible active sites. More importantly, this architecture is deliberately designed to function synergistically: Its high adsorption capacity rapidly preconcentrates target pollutants from the bulk solution onto the catalyst surface, thereby overcoming mass transfer limitations and providing a locally high concentration of reactants for the subsequent photocatalytic reactions. Meanwhile, the tailored interstitial doping addresses the intrinsic electronic limitations at their origin [43].

Therefore, this work serves to validate a predictive doping paradigm grounded in multi-dimensional atomic mismatch. It demonstrates how this principle can be leveraged to rationally design advanced photocatalysts. By synergistically coupling the electronic structure engineering (for enhanced light harvesting and charge separation) with a 3D hierarchical architecture (for abundant active sites and efficient adsorption-enabled preconcentration), we construct a highly efficient system that overcomes fundamental limitations in light absorption, charge recombination, and mass transfer. These synergistic effects culminate in outstanding visible-light photocatalytic detoxification of doxorubicin, achieving a high degradation efficiency of 96.9 % within 30 min, accompanied by notable total organic carbon (TOC) removal and a substantial reduction in ecotoxicity, as evidenced by zebrafish embryo assays. This study underscores the transformative potential of combining predictive material design with multi-scale structural engineering to concurrently optimize electronic properties and active site availability for constructing high-performance synergistic adsorption-photocatalysis systems for sustainable environmental remediation.

Fig. 1a schematically illustrates the synthesis of ultrathin 3D cross-linked B-doped Nb_2O_5 (BNO). This synthesis was designed to implement the atomic-mismatch-guided doping strategy. Initially, $NbCl_5$ was hydrolyzed under weak alkaline conditions, followed by hydrothermal treatment at 180 °C to form niobic acid layers. The obtained precipitate was then dispersed in an aqueous solution of H_3BO_3. The selection of B^{3+} from H_3BO_3, which possesses a much smaller ionic radius and a lower valence state compared to Nb^{5+}, was pivotal in creating the atomic mismatch necessary to steer the doping process. After freeze-drying and subsequent calcination, the final B-doped Nb_2O_5 material with an ultrathin 3D

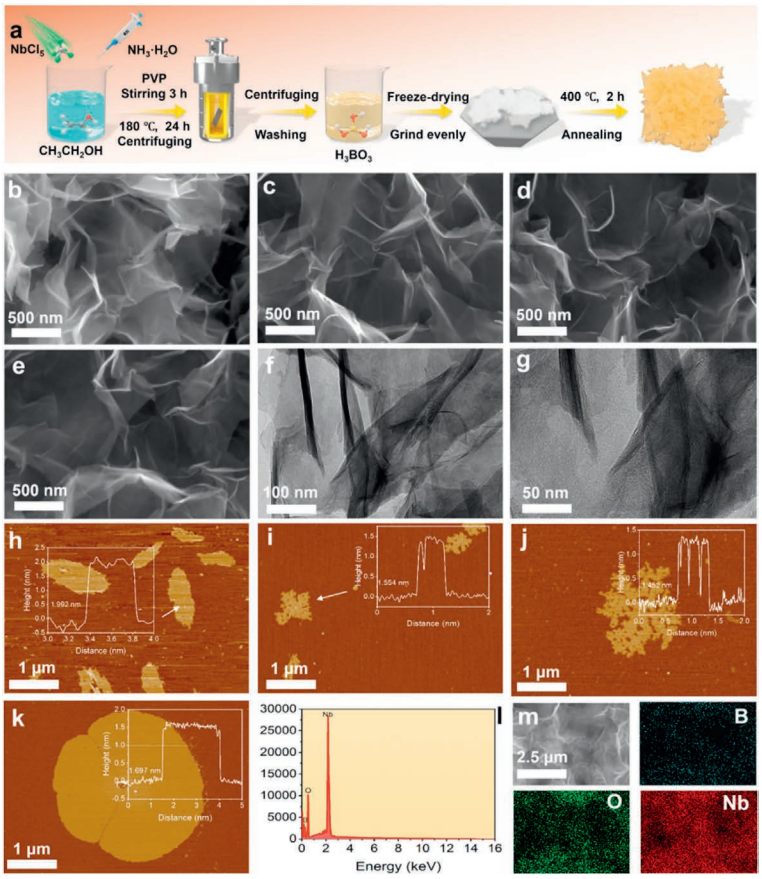


Fig. 1. (a) Schematic diagram of the fabrication process for BNO samples. SEM images of (b) Nb_2O_5, (c) BNO-1, (d) BNO-2, and (e) BNO-3. (f, g) TEM images of BNO-2 and AFM images of (h) Nb_2O_5, (i) BNO-1, (j) BNO-2, and (k) BNO-3. (l) EDS spectrum and (m) corresponding elemental mapping images of BNO-2.

cross-linked structure was obtained. The morphology and structural characteristics of the pure Nb_2O_5 and BNO samples were investigated by scanning electron microscopy (SEM), transmission electron microscopy (TEM), and atomic force microscopy (AFM). As shown in Figs. 1b-e, all samples exhibit a 3D architecture that cross-links and self-assembles from ultrathin nanosheets. Notably, with increasing boron doping levels, the cross-linking degree of the material is progressively enhanced, resulting in a more loosely arranged and porous superstructure. The observed structural evolution is responsible for the increased specific surface area, which provides abundant active sites for the catalytic reaction and leads to enhanced catalytic activity and stability. The formation of this 3D interconnected network of ultrathin nanosheets is directly visualized in the TEM images of the BNO-2 catalyst (Figs. 1f and g, Fig. S1 in Supporting information). The ultrathin nature was quantitatively confirmed by AFM (Figs. 1h-k), which measured thicknesses of 1.99, 1.55, 1.45, and 1.70 nm for Nb_2O_5, BNO-1, BNO-2, and BNO-3, respectively. This trend indicates that moderate B doping effectively reduces the nanosheet thickness, which can be attributed to the role of H_3BO_3 in promoting the separation of layered structures during thermal treatment, consequently maximizing the exposure of active sites [47]. When the B doping level is excessively high (BNO-3), the B_2O_3 formed from H_3BO_3 pyrolysis deposits on the Nb_2O_5, which then leads to a consequent increase in thickness. Furthermore, the corresponding elemental mapping (Figs. 1l and m) demonstrates the homogeneous spatial distribution of Nb, O, and B within the Nb_2O_5 framework, offering preliminary evidence for the successful and uniform boron incorporation [48].

The structural properties were further analyzed by N_2 adsorption-desorption measurements. Fig. 2a shows that all catalysts exhibit type IV isotherms accompanied by an H3 hysteresis loop, characteristic of mesoporous materials. Pore size distribution analysis reveals that B doping induces a discernible shift in the primary pore diameter from approximately 30 nm in pristine Nb_2O_5 to a broader distribution centered around 35 nm in the BNO samples. The specific surface areas and total pore volumes, summarized in Table S1 (Supporting information), follow the sequence of BNO-2 > BNO-1 > BNO-3 > Nb_2O_5. This initial increase can be ascribed to the release of gases (*e.g.*, water vapor) during the decomposition of boric acid, which etches and creates more pores within the structure [49]. The subsequent decrease for BNO-3 is likely due to pore blockage or surface coverage by excess boron species, potentially in the form of B_2O_3 aggregates. The X-ray diffraction (XRD) patterns in Fig. 2b show that all samples are largely amorphous, which is attributable to the relatively low calcination temperature of 400 °C. The calcination temperature of 400 °C was carefully optimized to preserve the ultrathin porous architecture while enabling effective boron incorporation. Niobic acid precursors typically undergo dehydration and structural ordering between 300 °C and 500 °C. At temperatures below 400 °C, the material may retain excessive hydroxyl groups and remain largely amorphous, which can impede charge transport. At 400 °C, the resulting Nb_2O_5 typically exhibits a "*pseudo*–amorphous" or low–crystalline phase that is favorable for exposing abundant surface sites while retaining sufficient electronic conductivity for photocatalysis. Moreover, H_3BO_3 decomposes gradually in the range of approximately 300–450 °C. A temperature of 400 °C ensures complete decomposition of the boron precursor while allowing controlled diffusion of boron species into the interstitial sites of Nb_2O_5. Experimental evidence indicates that H_3BO_3 fully

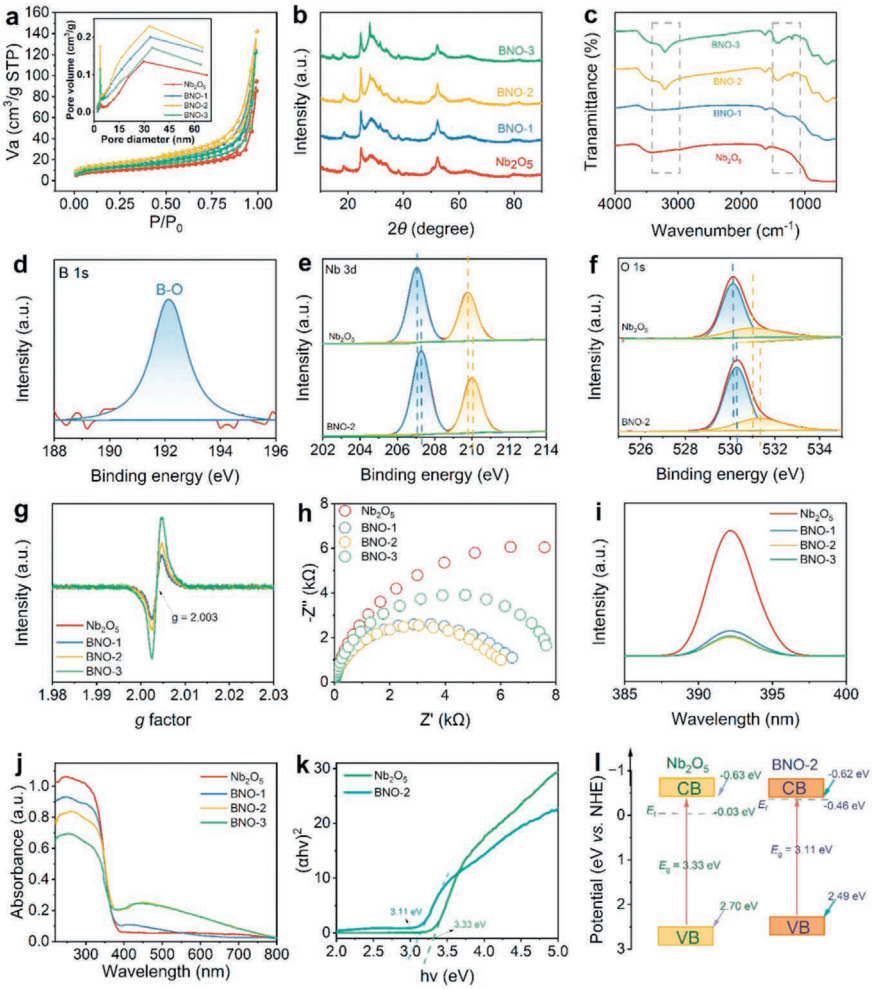


Fig. 2. Physicochemical properties of the Nb_2O_5 and BNO catalysts. (a) N_2 sorption isotherms (inset: pore size distribution), (b) XRD patterns, and (c) FTIR spectra. (d-f) High-resolution XPS spectra of B 1s, Nb 3d, and O 1s levels for BNO-2 and Nb_2O_5. (g) EPR spectra, (h) PL spectra, (i) EIS Nyquist plots, (j) UV–vis DRS spectra, (k) Tauc plots, and (l) a schematic of the band structure alignment.

evaporates at 450 °C, implying that excessively high temperatures could trigger rapid boron segregation or evaporation. Therefore, 400 °C represents a balanced condition that maintains the ultrathin porous Nb_2O_5 framework and achieves effective interstitial boron doping. A characteristic peak near 14.7° in BNO-3 corresponds to the formation of B_2O_3, indicating that excess boron may exist as B_2O_3 on the Nb_2O_5 surface. This finding indicates that at high doping concentrations, excess boron beyond the interstitial solubility limit segregates to form separate B_2O_3 phases on the surface. Fourier transform infrared (FTIR) spectroscopy is used to probe the functional groups in Nb_2O_5 and BNO samples. As shown in Fig. 2c, the absorption bands in the region of 500–1000 cm^{-1} are attributed to Nb-O and Nb=O vibrations [50]. With increasing boron doping, two new features become prominent: A band at 3208 cm^{-1}, corresponding to B-OH stretching vibrations, and a broad band in the 1142–1495 cm^{-1} region, associated with B-O stretching modes. This provides direct spectroscopic evidence for the presence of boron-oxygen bonds within the material.

X-ray photoelectron spectroscopy (XPS) was employed to further investigate the surface chemical states and elemental composition of the prepared samples. The survey spectrum (Fig. S2 in Supporting information) confirms the presence of Nb, O, and B in the BNO-2 sample. The high-resolution B 1s spectrum (Fig. 2d) exhibits a single peak at a binding energy of 192.1 eV, characteristic of B-O bonds, indicating the formation of B_2O_3-like species [51]. Since no other characteristic peaks are observed, it can be inferred that boron largely exists in the form of B_2O_3 and is evenly distributed in Nb_2O_5 lattice interstices, a conclusion reinforced by Table S2 (Supporting information). This conclusion is further supported by the elemental mapping and the visual observation of the sample's color: The distinct yellow hue of the BNO samples, contrasting with the white color of pure Nb_2O_5 and B_2O_3, serves as a simple yet convincing indicator of successful boron doping into the Nb_2O_5 lattice, rather than mere surface attachment. The high-resolution Nb 3d spectra (Fig. 2e) show the characteristic doublet for Nb^{5+} in both samples [52]. The positive shifts observed in the Nb 3d and O 1s core-levels of BNO-2 (Figs. 2e and f) indicate a decrease in the electron density surrounding the Nb and O atoms. This serves as a clear spectroscopic signature of electron transfer from the Nb-O framework to the interstitial boron species, which act as electron acceptors due to their intrinsic electron deficiency (B^{3+}). This redistribution of electrons has two critical implications for charge carrier dynamics: It establishes a local electric field that promotes the spatial separation of photogenerated electron-hole pairs. More importantly, the electron-deficient interstitial boron species effectively trap photogenerated electrons. Therefore, the XPS results not only confirm the success of the doping process but also provide key evidence for the boron-induced electronic modulation, which lies at the core of the enhanced photocatalytic activity.

Raman spectroscopy (Fig. S3 in Supporting information) provides additional evidence for the successful incorporation of boron. The characteristic bands of Nb_2O_5 at 294 cm^{-1} (bending vibrations of Nb-O-Nb) [17] and 637 cm^{-1} (amorphous $Nb_2O_5{\cdot}nH_2O$) [53] are observed to shift upon boron doping. A band around 890 cm^{-1} corresponds to the stretching of the Nb=O surface group [54]. This perturbation of the Nb-O vibrational modes confirms that the introduction of boron disrupts the local lattice structure, aligning with the interstitial doping model. Moreover, the presence of unpaired electrons in the catalysts was characterized by electron paramagnetic resonance (EPR) spectroscopy, and all catalysts display a Lorentzian line shape with a *g*-factor of 2.003 (Fig. 2g). The signal intensity increases markedly with higher boron content, indicating a substantial increase in the concentration of unpaired electrons. This suggests that interstitial B doping effectively generates paramagnetic centers or traps that can capture charge carriers, thereby potentially suppressing their recombination.

To gain deeper insight into the charge separation efficiency and transfer dynamics, electrochemical impedance spectroscopy (EIS) and photoluminescence (PL) spectroscopy were conducted. The Nyquist plots from EIS (Fig. 2h) show that all BNO catalysts exhibit a smaller semicircular arc radius compared to pure Nb_2O_5, with BNO-2 possessing the smallest radius. This indicates a significantly decreased charge-transfer resistance and the most efficient electron-hole separation in the optimally doped sample. This conclusion is strongly supported by the PL spectra (Fig. 2i), where the emission intensity, originating from the recombination of photogenerated carriers, is substantially quenched in the BNO samples. The BNO-2 catalyst exhibits the weakest PL signal, demonstrating the most effective suppression of charge carrier recombination. These results collectively affirm that the interstitial boron doping creates favorable pathways and trapping sites for charge carriers, thereby facilitating their separation and transfer, which is a cornerstone of the enhanced photocatalytic activity [55,56].

The optical properties and electronic band structures of the samples were critically examined to understand the essence of the electronic structure engineering. The ultraviolet-visible (UV–vis) diffuse reflectance spectra (Fig. 2j) reveal that pure Nb_2O_5 absorbs primarily in the UV region, with negligible visible light absorption. In stark contrast, all B-doped samples display a pronounced enhancement in absorption across the visible spectrum (400–800 nm). This dramatic extension of the absorption edge is a direct visual manifestation of the successful band structure modification induced by doping. The Tauc plots derived from the spectra (Fig. 2k) quantify this effect, showing a reduction in the bandgap energy from 3.33 eV for Nb_2O_5 to 3.11 eV for BNO-2. To further deconvolute the band structure alterations, the positions of the valence band (VB) and the conduction band (CB) were determined by Mott-Schottky (Fig. S4 in Supporting information) and XPS valence band spectra measurements (Fig. S5 in Supporting information). The calculated energy band alignment diagram is depicted in Fig. 2l and summarized in Table S3 (Supporting information). The data indicates that interstitial boron doping induces an upward shift of the Fermi level and modifies the positions of both the valence and conduction bands. This optimized band structure not only narrows the bandgap for enhanced light harvesting but also favorably positions the band edges to facilitate the generation of superoxide radicals, which is consistent with the subsequent mechanistic studies. The collective characterization data from EPR, EIS, PL, and UV–vis provide compelling and multi-faceted evidence that the atomic-mismatch-guided interstitial boron doping effectively engineers the electronic structure of Nb_2O_5, leading to optimized optical absorption, superior charge separation, and tailored redox potentials.

To gain a fundamental understanding of the observed enhancement in photocatalytic performance, we employed density functional theory (DFT) calculations to probe the electronic structure modulation induced by interstitial boron doping. The optimized structural models for Nb_2O_5 and BNO-2 are presented in Fig. S6 (Supporting information) and Fig. 3a, respectively. Figs. 3b and c illustrate the density of states (DOS), revealing that the valence band maximum (VBM) of pristine Nb_2O_5 is primarily composed of O 2p orbitals, while the conduction band minimum (CBM) is dominated by Nb 4d orbitals. Upon interstitial B doping, a significant electronic structure modulation occurs: Strong orbital hybridization among Nb-d, O-p, and B-s states is observed near the CBM. This hybridization increases the density of states at the conduction band edge and effectively narrows the bandgap, which aligns with our experimental UV–vis results. This modulation provides more channels for electronic transitions and enhances the photoexcitation capability under visible light. Further analysis of the electron localization function (ELF) offers deep insight into the changes in chemical bonding and electron distribution. As depicted in Figs. 3d and e, the electron density around O atoms is generally high in both samples. However, BNO-2 exhibits a distinct electron delocalization phenomenon and stronger electronic interactions compared to Nb_2O_5. This suggests that the interstitial B species effectively withdraw electron density and modify the charge distribution surrounding the host atoms, creating a more favorable electronic environment for charge transfer.

Beyond the ground-state electronic structure, the dynamics of photogenerated charge carriers are pivotal to photocatalytic efficiency. We first investigated the excitonic behavior, as the dissociation of photogenerated excitons into free carriers is a critical initial step [57]. The temperature-dependent PL spectra (Fig. S7 in Supporting information) show a gradual decrease in intensity from 80 K to 300 K for all samples, consistent with thermally activated exciton dissociation [58]. By applying the Arrhenius equation to the integrated PL intensity (Figs. 3f and g), the exciton binding energy (E_b) was determined. The E_b of BNO-2 (46.7 meV) is considerably lower than that of Nb_2O_5 (64.1 meV), indicating a significantly reduced energy barrier for exciton dissociation into free electrons and holes. This facilitates the initial generation of free charge carriers, which is a crucial advantage for driving photocatalytic reactions.

To directly track the relaxation pathways of these free charge carriers, femtosecond transient absorption (fs-TA) spectroscopy was employed in Figs. 3h and i and Figs. S8 and S9 (Supporting information) [59], The time-dependent 3D contour plots (Figs. 3h and i) show negative signals attributed to ground-state bleaching and positive signals arising from excited-state absorption (ESA) [60,61]. Notably, the ESA signal is more pronounced in BNO-2, suggesting a larger population of long-lived excited-state carriers [62]. The decay kinetics at the maximum fs-TA absorption were fitted (Fig. S9), yielding two lifetime components: A fast lifetime (τ_1) associated with the initial trapping or transfer of carriers, and a slow lifetime (τ_2) related to the recombination or reaction of trapped carriers [63]. A critical finding is that BNO-2 exhibits a shorter τ_1 (131.96 ps) than Nb_2O_5 (141.68 ps), implying more rapid charge trapping or transfer. More importantly, BNO-2 demonstrates a dramatically prolonged τ_2 (2775.64 ps) compared to Nb_2O_5 (859.56 ps). This combination of a shorter τ_1 and a longer τ_2 signifies that in BNO-2, photogenerated carriers are rapidly captured into traps and subsequently exhibit a much longer lifetime for participating in surface redox reactions. Based on the above analysis, it is demonstrated that the atomic-mismatch-guided interstitial boron doping serves as the foundational strategy that effectively engineers the electronic structure of Nb_2O_5 by narrowing the bandgap and enhancing electron delocalization. Subsequently, this tailored electronic structure optimizes the charge carrier dynamics by lowering the exciton binding energy for efficient free carrier generation and, most critically, establishing long-lived shallow traps that drastically prolong the charge

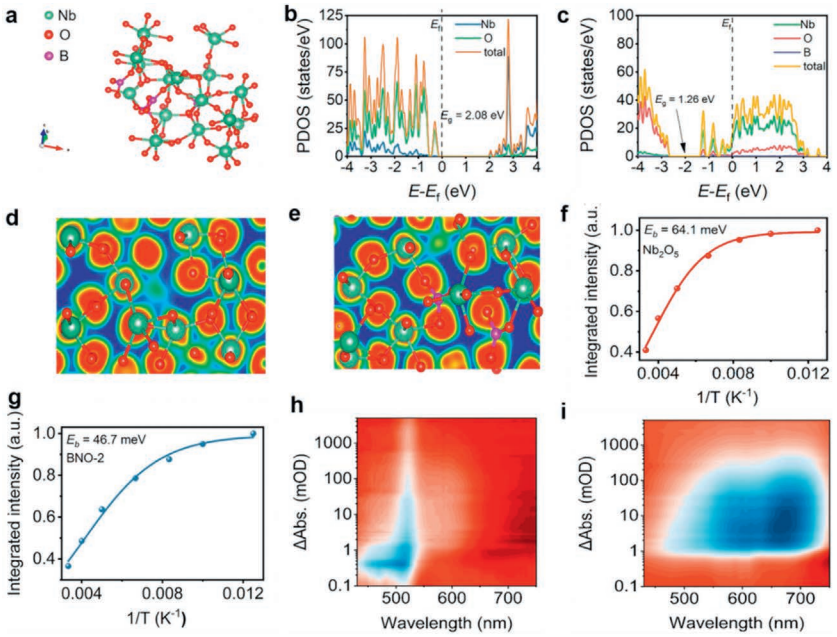


Fig. 3. Structural model of (a) BNO-2. DOS of (b) Nb_2O_5 and (c) BNO-2. Electron localization function (ELF) distribution diagrams (red: higher values, blue: lower values) of (d) Nb_2O_5 and (e) BNO-2. Integrated PL emission intensity as a function of temperature ($\lambda_{excitation} = 316$ nm) for (f) Nb_2O_5, (g) BNO-2. (h, i) Time-dependent 3D contour plots of fs-TAS.

separation lifetime. These synergistic effects collectively contribute to achieving superior photocatalytic activity.

The efficacy of the electronic structure-engineered B-doped Nb_2O_5 catalysts was evaluated through the photocatalytic degradation of DOX under visible light irradiation. As shown in Fig. 4a, control experiments confirmed the high stability of DOX, with only 7.8 % degradation observed in the absence of any catalyst. Notably, the degradation process exhibited a distinct two-stage mechanism: An initial rapid adsorption phase during the dark period, followed by a pronounced visible-light-driven photocatalytic degradation phase. The optimized BNO-2 catalyst demonstrated exceptional adsorption capacity due to its 3D porous architecture, achieving 77.4 % adsorption efficiency during the dark phase. Upon visible light irradiation, an additional 19.5 % of DOX was degraded by the photocatalytic reaction, leading to and reaching a total removal rate of 96.9 % within 30 min. This net photocatalytic degradation represents a significant contribution, especially considering the high initial adsorption, and underscores the synergistic role of adsorption and photocatalysis in the overall removal process. This remarkable performance represents a 2.5-fold enhancement compared to pristine Nb_2O_5, directly validating the success of our atomic-mismatch-guided doping strategy in engineering an efficient photocatalytic system. The enhanced performance can be attributed to the synergistic effects arising from the electronic structure modulation and the structural advantages. Featuring a 3D cross-linked framework, the material offers a high density of accessible active sites for both adsorption and catalytic reactions; concurrently, interstitial boron doping boosts its visible-light absorption and charge separation efficiency.

Comparative analysis revealed that both adsorption and photocatalytic degradation efficiencies of the BNO catalysts substantially exceeded those of pure Nb_2O_5, with BNO-2 exhibiting the optimal performance. However, excessive boron loading (BNO-3) resulted in diminished activity, which can be attributed to the induced defects that serve as charge recombination centers. Kinetic analysis further confirmed these observations (Fig. S10 in Supporting information), revealing that BNO-2 possessed an apparent rate constant of 45.4×10^{-3} min^{-1}. This represents a 4.2-fold enhancement over the value of 10.9×10^{-3} min^{-1} measured for Nb_2O_5. It is important to note that the kinetic constant was calculated based on the photocatalytic degradation phase after adsorption equilibrium, thus reflecting the genuine photocatalytic activity. Furthermore, the data compiled in Table S4 (Supporting information) corroborate the superior performance of the BNO series. Notably, BNO-2 exhibited an adsorption efficiency of 77.4 % (2.4 times that of pure Nb_2O_5) and an overall degradation rate of 96.9 %, which is twice as high as that of the undoped catalyst. This distinct two-phase process is not a limitation but a designed advantage: The 3D porous network first acts as a highly efficient adsorbent, rapidly concentrating DOX molecules from the bulk solution onto the catalyst surface, thereby drastically increasing the local concentration of the pollutant at the very sites where reactive oxygen species are generated under illumination. This “enrichment-then-destruction” strategy effectively circumvents mass transfer limitations commonly encountered in heterogeneous photocatalysis, ensuring that the photogenerated radicals react with their target more efficiently. To further elucidate the photocatalytic performance and demonstrate the extent of contaminant mineralization, the TOC variation of the DOX solution during the degradation process was also analyzed. As shown in Fig. S11 (Supporting information), the BNO-2 sample achieved a TOC removal rate of 71.2 % after 90 min of photocatalytic reaction, indicating that the adsorbed DOX was not merely concentrated but progressively decomposed into smaller molecules and ultimately mineralized. This further confirms the highly efficient pollutant degradation and mineralization performance of this adsorption-degradation synergistic catalytic system.

To establish optimal operational parameters, we systematically investigated the influence of key environmental factors on the degradation efficiency. The initial DOX concentration exhibited an inverse relationship with degradation efficiency (Fig. 4b and Fig. S12 in Supporting information), where reducing the concentration from 60 mg/L to 20 mg/L enhanced the removal rate from 51.3 % to 99.8 %, with corresponding rate constants increasing from 11.3×10^{-3} to 55.1×10^{-3} min^{-1}. A positive correlation was observed between the catalyst dosage (5–30 mg) and the degradation performance (Fig. 4c and Fig. S13 in Supporting information),

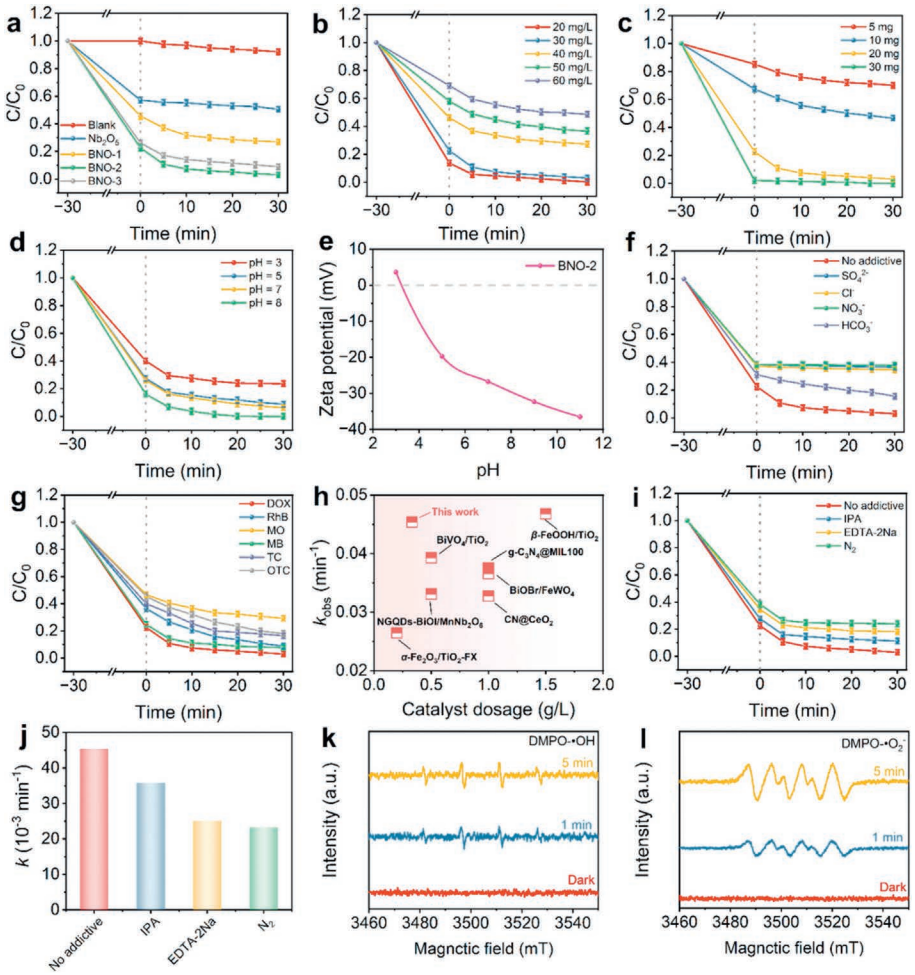


Fig. 4. Effect of various parameters on DOX degradation: (a) Catalyst type, (b) initial DOX concentration, (c) BNO-2 dosage, (d) solution pH, (e) corresponding zeta potential, (f) coexisting ions, and (g) different pollutants. (h) Performance comparison with previously reported catalysts. (i, j) Scavenger experiments revealing active species. Spin-trapping EPR signal for the detection of ·OH (k) and $\cdot O_2^-$ (l), respectively.

where the rate constant increased accordingly from 5.1×10^{-3} to 75.5×10^{-3} min^{-1}. These trends reflect the fundamental relationship between active site availability, radical generation capacity, and overall process efficiency. Solution pH emerged as a critical parameter governing the degradation efficiency through its influence on surface charge and molecular speciation [64,65]. As illustrated in Figs. 4d and e and Fig. S14 (Supporting information), the degradation efficiency increased progressively from 76.4 % to 100.0 % as the pH increased from 3 to 8, with rate constants rising from 16.1×10^{-3} to 36.0×10^{-3} min^{-1}. This behavior can be rationalized by considering the zero-point charge ($pH_{zpc} = 3.2$) of BNO-2 and the acid-base characteristics of DOX ($pH_{zpc} = 8.2$) [66]. Under acidic conditions (pH < 3.2), electrostatic repulsion between the positively charged catalyst surface and protonated DOX molecules limits adsorption efficiency. As the pH increases, the catalyst surface becomes negatively charged while DOX remains cationic, resulting in enhanced electrostatic attraction and consequently improved degradation performance.

The impact of common inorganic anions on the degradation process was investigated to assess practical applicability, with all anions tested at a concentration of 10 mmol/L. As shown in Fig. 4f and Fig. S15 (Supporting information), all tested anions (Cl^-, HCO_3^-, SO_4^{2-}, and NO_3^-) exhibited inhibitory effects to varying degrees. In the presence of Cl^-, HCO_3^-, NO_3^-, and SO_4^{2-}, the degradation rates of DOX were 65.3 %, 84.3 %, 62.2 %, and 63.5 %, respectively, with corresponding kinetic constants of 17.1×10^{-3}, 30.2×10^{-3}, 15.5×10^{-3}, and 16.2×10^{-3} min^{-1}. At the tested concentration of 10 mmol/L, Cl^-, NO_3^-, and SO_4^{2-} were found to primarily inhibit the photocatalytic degradation process through radical scavenging mechanisms [67], whereas HCO_3^- predominantly suppressed the reaction by competing with DOX for adsorption sites on the catalyst surface. More specifically, Cl^- at this concentration reacts with ·OH to generate less reactive chlorine radicals, while sulfate and nitrate-related species consume ·OH, leading to a notable decline in the overall degradation efficiency [68]. The inhibitory effect of HCO_3^- is attributed to its competition with DOX molecules for the limited active sites, which reduces DOX adsorption and consequently impairs the photocatalytic performance. The BNO-2 catalyst demonstrated remarkable versatility in degrading various organic pollutants beyond DOX (Fig. 4g), showing high efficiency for rhodamine B (RhB), tetracycline (TC), and oxytetracycline (OTC). Stability tests revealed excellent recyclability (Fig. S16 in Supporting information), with the DOX removal rate maintaining 85.9 % after five consecutive cycles, representing only an 11.0 % decrease from the initial performance. Comparative analysis with previously reported catalysts (Fig. 4h and Table S5 in Supporting information) further highlighted the superior performance of our material, underscoring the advantages of the atomic-mismatch-guided doping strategy. As compiled in Table S5, BNO-2 achieves a 96.80 % degradation within 30 min under visible light, which translates to a high apparent rate constant of 45.4×10^{-3} min^{-1}. This performance is notable even when nor-

malized for catalyst dosage and pollutant concentration. For instance, compared to recently reported prominent catalysts such as BiOBr/$FeWO_4$ (90.4 % in 60 min), α-Fe_2O_3/TiO_2-FX (95.75 % in 120 min), and g-C_3N_4@MIL-100 (82.8 % in 30 min), BNO-2 demonstrates a superior or comparable degradation efficiency within a significantly shorter time frame or with a lower catalyst loading. More importantly, the synergy between enhanced adsorption (77.4 %) and efficient photocatalysis in our system is not commonly highlighted in many comparative studies that focus solely on photocatalytic degradation percentages. This dual functionality, combined with the rapid kinetics, positions BNO-2 as a highly competitive candidate for the remediation of antibiotic-contaminated water.

Building upon the engineered electronic structure of the catalyst, systematic trapping experiments were designed to decipher the primary reactive species governing the degradation process. To probe the primary reactive species, scavenging experiments were conducted using isopropanol (IPA) for ·OH, EDTA-2Na for h^+, and N_2 purging to eliminate $\cdot O_2^-$. As depicted in Figs. 4i and j, the presence of EDTA-2Na and IPA caused only a marginal suppression of the degradation rate, implying that h^+ and ·OH are not the predominant active species. Conversely, a pronounced decrease in the rate constant under N_2 atmosphere conclusively identifies $\cdot O_2^-$ as the dominant radical in the degradation process. However, in the presence of N_2, the DOX degradation rate is markedly reduced, indicating that $\cdot O_2^-$ plays a dominant role in the degradation process. To further corroborate these findings, EPR measurements were employed to directly detect the generation of reactive species during photocatalysis. As shown in Figs. 4k and l, no discernible signals for either radical were detected in the dark. However, under visible-light irradiation, distinctive EPR signals for both ·OH and $\cdot O_2^-$ emerged, with their intensities progressively enhancing with prolonged irradiation time. Notably, the signal intensity increase was substantially more pronounced for $\cdot O_2^-$ than for ·OH, providing direct spectroscopic evidence that supports the trapping experimental results and reinforces the conclusion regarding the crucial role of $\cdot O_2^-$ in the degradation mechanism. The predominance of $\cdot O_2^-$ generation is consistent with the electronic structure engineering achieved through interstitial boron doping, which facilitates efficient electron transfer to molecular oxygen and enhances charge separation efficiency.

To gain deeper insight into the molecular-level degradation mechanism, DFT calculations were performed to identify the vulnerable sites within the DOX molecule. Following the optimized structure of DOX (Fig. 5a), the associated electrostatic potential (ESP) was calculated and plotted on its electron density surface (Fig. 5b). This ESP map furnishes critical insights into local reactivity [69]. Nucleophilic sites, which are electron-rich and appear in blue, possess negative ESP values. Conversely, electrophilic sites, characterized by positive ESP and a red coloration, represent regions of low electron density. Specific analysis identified C8 and O28 as nucleophilic sites, while the O36 and O23 atoms within the hydroxyl groups were recognized as electrophilic sites. The pronounced electrophilicity around the oxygen atoms suggests their susceptibility to electron-stripping reactions. Fig. 5c displays the electron density of the frontier orbitals. The HOMO is mainly found on the central benzene ring, thereby pinpointing it as the primary region for electrophilic reactions. In contrast, the LUMO is concentrated on the central linking ring, marking it as the target for nucleophilic attack. The resulting HOMO-LUMO energy gap was calculated to be 3.006 eV. This analysis is complemented by the Fukui function, where elevated values (Table S6 in Supporting information) serve as a well-established indicator of atoms with heightened chemical reactivity [70]. Fukui function analysis reveals that C8, C11, O27, and O28 possess high f^- values, rendering them more susceptible to electrophilic attack [71], whereas C7, C10, O24, and O25 have higher f^+ values, making them more prone to nucleophilic attack [72]. Notably, O24, O25, O27, and O28 are identified as primary sites for ·OH attack due to their higher f^0 values [73].

Based on the comprehensive LC-MS analysis (Fig. S17 and Table S7 in Supporting information) integrated with DFT calculations, three potential degradation pathways for DOX were elucidated, with thirteen intermediate products identified. As illustrated in Fig. 5d, in pathway I, DOX (MW = 543) undergoes hydrolysis initiated by the attack of $\cdot O_2^-$ to form **P1** (MW = 414), which is subsequently reduced to **P2** (MW = 416) *via* a reduction reaction [74,75]. In pathway II, DOX loses its amino sugar moiety, resulting in fragmentation and the formation of either sugar fragment **P3** (MW = 396) or **P4** (MW = 396) [76,77]. **P3** then undergoes a dehydration reaction to generate **P5** (MW = 336) [74,75]. Alternatively, **P3** can also be converted to **P6** (MW = 380) through the removal of a hydroxyl group [78]. **P6**, after losing $C_2H_4O_2$, is further converted to **P7** (MW = 320), and finally **P7** undergoes C–C bond cleavage to produce **P8** (MW = 160) [78]. In pathway III, DOX loses its amino sugar moiety due to glycosidic bond cleavage, generating protonated sugar **P9** (MW = 147) or **P10** (MW = 147) [78,79]. Subsequently, **P9** or **P10** undergoes dehydration reactions to yield **P11** (MW = 129) or **P12** (MW = 129), respectively [79]. Among the entire degradation pathways, Pathway I dominates the process, which can be reasonably explained by the tailored electronic structure of the BNO-2 catalyst. As confirmed by our band structure analysis (Fig. 2l), interstitial boron doping induces an upward shift of the conduction band (CB) position. This optimized CB edge (−0.62 V *vs.* NHE) is more negative than the redox potential of $O_2/\cdot O_2^-$ (−0.33 V *vs.* NHE), thermodynamically favoring the reduction of adsorbed molecular oxygen (O_2) to $\cdot O_2^-$ by photogenerated electrons. Meanwhile, efficient charge separation and prolonged carrier lifetime, as verified by PL and fs–TA spectroscopy, ensure a sufficiently high electron flux available for O_2 reduction. Consequently, $\cdot O_2^-$ becomes the most abundant reactive oxygen species on the catalyst surface, rendering Pathway I the kinetically most favorable route.

To evaluate the environmental safety and practical application potential of the photocatalytic system, the toxicity evolution during DOX degradation was systematically investigated. We employed the Toxicity Estimation Software Tool (T.E.S.T.) to predict the potential ecotoxicity of the transformation products generated from DOX throughout the photocatalytic reaction, with results focusing on fathead minnow LC_{50} (96 h), daphnia magna LC_{50} (48 h), and developmental toxicity data (Figs. 6a-c and Table S8 in Supporting information). As shown in Fig. 6a, the fathead minnow LC_{50} values of **P9**, **P10**, **P11**, and **P12** are all exceeded 100 mg/L, indicating a substantial reduction in acute toxicity compared to the parent DOX compound. Furthermore, as illustrated in Fig. 6b, the daphnia magna LC_{50} for DOX is 11.56 mg/L, classifying it as "harmful". Remarkably, with the exception of **P5**, **P7**, and **P8**, all other degradation products exhibited significantly higher LC_{50} values, further confirming the considerable reduction in acute toxicity following photocatalytic treatment. Additionally, the developmental toxicity of the products presented in Fig. 6c decreases with the catalytic process, with product **P10** even classified as "developmentally non-toxic". Collectively, these computational predictions provide compelling evidence that the degradation products generated during the photocatalytic process possess substantially lower potential toxicity than the original drug molecule.

To experimentally validate the computational predictions and obtain more biologically relevant toxicity data, zebrafish embryos were selected as an *in vivo* aquatic model for toxicity assessment. The experimental protocol was reviewed and approved by the laboratory animal ethics committee of Henan Medical University. Dur-

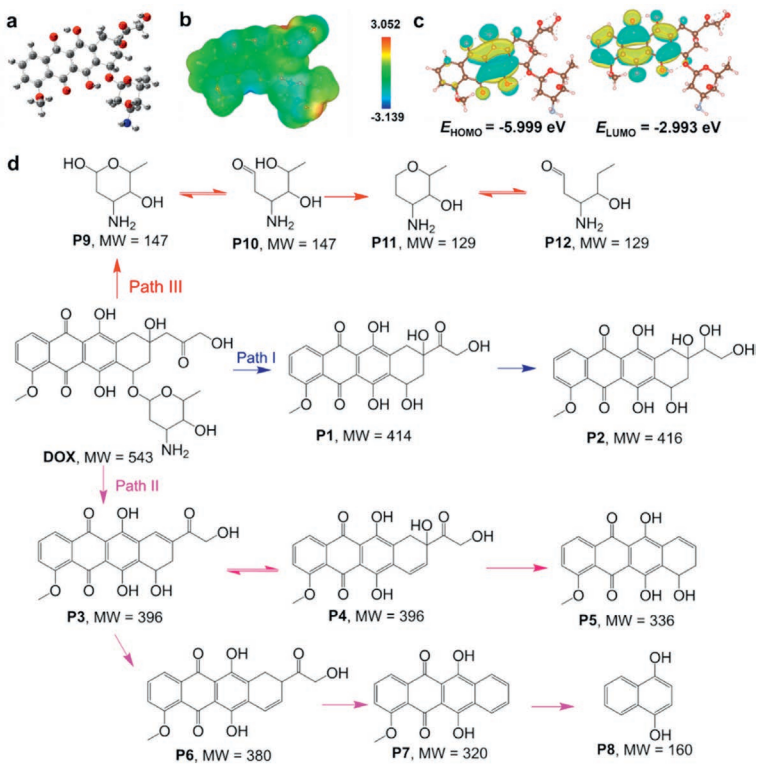


Fig. 5. (a) Optimized molecular geometry. (b) ESP surface map. (c) Distributions of the frontier molecular orbitals (HOMO and LUMO). (d) Proposed degradation pathways of DOX catalyzed by the BNO-2 system.

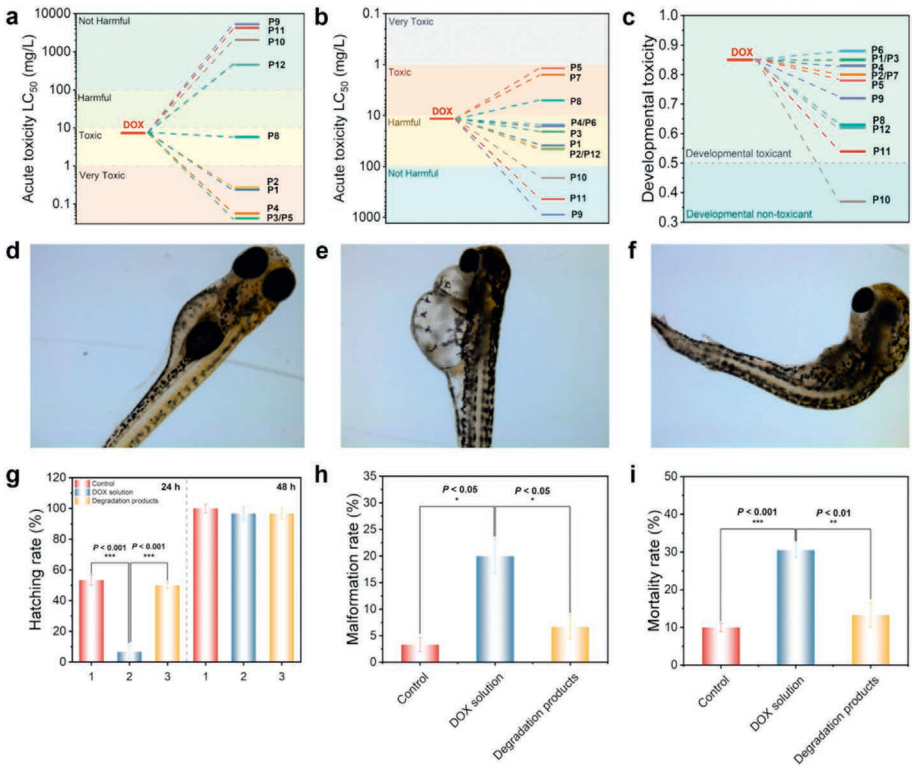


Fig. 6. Acute toxicity of DOX and its degradation products: (a) Fathead minnow LC_{50} (96 h), (b) Daphnia magna LC_{50} (48 h), (c) developmental toxicity. (d) Normal morphology, (e) pericardial edema morphology, and (f) scoliosis morphology of zebrafish. (g) Hatching rate, (h) deformity rate, and (i) mortality rate of zebrafish with DOX and its degradation products.

ing the experiment, all animals were treated humanely, and their pain and discomfort were minimized to the greatest extent possible. Figs. 6d-f illustrate representative morphologies of zebrafish observed during the toxicity experiments, including normal development, pericardial edema, and scoliosis. The experiments compared the effects of different solutions on zebrafish embryo hatching rates (Fig. 6g), revealing significant differences among the three treatment groups after 24 h of exposure. However, this distinction became less apparent after 48 h. This temporal pattern indicates that embryos exposed to DOX solutions exhibited delayed hatching, with markedly lower hatching rates at 24 h compared to both the control and degradation-product groups, suggesting that DOX solutions suppress embryo development and possess higher developmental toxicity. The comparison between the degradation-product group and the other groups showed insignificant differences when contrasted with the control group, while maintaining significant differences relative to the DOX solution, reinforcing the conclusion that DOX toxicity is substantially reduced upon degradation. As shown in Fig. 6h, the malformation rate in the DOX treatment group was significantly higher than those in both the control and degradation product groups, underscoring its higher teratogenic potential. Importantly, the malformation rate in the degradation solution group was comparable to that of the control group, indicating a considerable reduction in teratogenicity of the degradation products following photocatalytic treatment by the BNO catalyst. Additionally, analysis of zebrafish mortality rates (Fig. 6i) revealed that the DOX-treated group exhibited a significantly higher mortality rate than both the control and degradation-product groups, further validating the above conclusions. Therefore, the combined computational and experimental toxicity assessments demonstrate that the biotoxicity of intermediates in the degradation solution is significantly diminished through the utilization of BNO photocatalysts for pollutant degradation, confirming that the BNO catalytic system not only achieves superior DOX removal efficiency but also effectively mitigates degradation-related ecological toxicity.

The remarkable activity of the BNO catalyst, as detailed in previous sections, originates from the precise engineering of its electronic structure *via* an atomic-mismatch-guided interstitial boron doping strategy. This strategic approach induces multifaceted enhancements that collectively contribute to the exceptional degradation and detoxification efficiency observed for DOX. The enhanced catalytic mechanism primarily manifests in four interconnected aspects, all originating from the precisely controlled interstitial incorporation of boron: (1) The strategic interstitial boron doping effectively engineers the electronic structure of Nb_2O_5, primarily by narrowing the bandgap and introducing mid-gap states, which significantly enhances visible light absorption capacity; (2) the modified electronic structure facilitates the separation and transfer of photogenerated electron-hole pairs, dramatically improving charge carrier dynamics and reducing recombination losses; (3) the 3D cross-linked porous structure significantly increases the specific surface area and provides abundant accessible active sites, which enhances both the contact efficiency with DOX molecules and the adsorption capacity; (4) the synergistic combination of electronic structure modulation and morphological advantages creates an optimal environment for the generation of reactive oxygen species, particularly favoring the formation of $^{\bullet}O_2^-$ as the predominant reactive species.

As a promising photocatalytic material for degradation applications, the tailored electronic structure of the BNO catalyst facilitates the efficient promotion of valence band electrons to the conduction band under visible light, generating abundant photogenerated electron-hole pairs. Due to the electronic structure modulation induced by interstitial boron doping, the electrons in the conduction band subsequently readily reduce adsorbed oxygen molecules to generate $\cdot O_2^-$, while the holes in the valence band can oxidize water or hydroxide ions to produce ·OH. These reactive oxygen species, with $\cdot O_2^-$ identified as the dominant player in our mechanistic studies, serve as the critical components in the pollutant degradation and detoxification process. The atomic-mismatch-guided interstitial boron doping not only modifies the electronic structure but also introduces additional active sites to the catalyst and significantly enhances its adsorption capacity for reactant molecules, thereby comprehensively improving the photocatalytic performance. Furthermore, the tailored electronic structure of the BNO catalyst facilitates superior charge transfer. This not only promotes the efficient separation of photogenerated carriers but also minimizes their recombination loss, collectively leading to an acceleration of the organic pollutant degradation kinetics. In summary, the synergistic integration of the precisely engineered electronic structure *via* interstitial boron doping and the advantageous 3D hierarchical architecture creates a highly efficient photocatalytic system that maximizes light harvesting, promotes charge separation, facilitates targeted reactive species generation, and enhances mass transfer, collectively contributing to the superior performance in DOX degradation and detoxification.

This study successfully demonstrates the fabrication of a high-performance boron-doped Nb_2O_5 catalyst through a strategic dual-engineering approach. An innovative atomic-mismatch-guided interstitial doping strategy thermodynamically favors boron incorporation into lattice interstices, effectively engineering the electronic structure to narrow the bandgap, reduce exciton binding energy, and create long-lived charge traps. Concurrently, a deliberately constructed 3D cross-linked ultrathin architecture provides a high density of accessible active sites and exceptional adsorption capacity. The synergy between targeted electronic modulation and structural design for adsorption enrichment creates a powerful cooperative system. The three-dimensional and interconnected architecture observed by SEM and TEM was expected to confer high surface area and porosity. This was confirmed by N_2 physisorption analysis. Under visible light irradiation for 30 min, the degradation rate of DOX reached as high as 96.9 %, which is 2.5 times higher than that of pure Nb_2O_5. Through active species trapping experiments and EPR analysis, it was determined that the catalytic reaction is primarily driven by radicals, with h^+, $\cdot O_2^-$, and ·OH identified as the key active species in the DOX degradation process, among which $\cdot O_2^-$ plays a decisive role in the photocatalytic reaction. Furthermore, the degradation intermediates were characterized using LC-MS, and three possible degradation pathways for DOX were proposed. The toxicity of the intermediates formed during the degradation process was found to be lower than that of DOX, confirming the detoxification capability of this catalytic system. This work not only establishes a novel predictive doping paradigm but also exemplifies the rational design of synergistic adsorption-photocatalysis systems through concurrent nanoarchitectural and electronic engineering, offering a promising strategy for sustainable water remediation.

CRediT authorship contribution statement

Minghui Chen: Writing – original draft, Software, Methodology, Investigation, Data curation. **Lei An:** Writing – original draft, Supervision, Software, Methodology. **Kaiwei Wang:** Software, Methodology, Investigation. **Jianing Qian:** Supervision, Software, Methodology, Data curation. **Yuming Chen:** Methodology, Data curation. **Xingtao Xu:** Writing – review & editing, Supervision, Software, Methodology, Investigation. **Tianjun Ni:** Writing – review & editing, Writing – original draft, Software, Resources, Project administration. **Dong Liu:** Writing – review & editing, Writing – original draft, Supervision, Project administration, Data curation.

Declaration of competing interest

The authors declare that they have no known competing financial interests or personal relationships that could have appeared to influence the work reported in this paper.

Acknowledgments

This work was financially supported by the Science and Technology Development Project of Henan Province (No. 252102320094), Natural Science Foundation of Henan Province (Nos. 252300423128 and 242300421303), Key Research Project of Higher Education Institutions in Henan Province (No. 25A610003), Starting Research Fund of Xinxiang Medical University (No. XYBSKYZZ201911), and Research Foundation for Distinguished Professor's Team of Henan Medical University (No. 505527).

Supplementary materials

Supplementary material associated with this article can be found, in the online version, at doi:10.1016/j.cclet.2026.112794.

References

[1] C.Y. Ojemaye, L. Petrik, Environ. Pollut. 252 (2019) 562–572.
[2] R.B. González-González, P. Sharma, S.P. Singh, et al., Sci. Total Environ. 821 (2022) 153329.
[3] C.S. Pereira, M. Kelbert, N.A. Daronch, et al., Appl. Microbiol. Biot. 104 (2020) 23–31.
[4] S. Santana-Viera, P. Hernández-Arencibia, Z. Sosa-Ferrera, et al., J. Chromatogr. B 1110-1111 (2019) 124–132.
[5] F. Luan, Y. Cui, R. Huang, Z. Yang, et al., Sci. Rep. 15 (2025) 3223.
[6] X. Weng, L. Ma, M. Guo, et al., Chem. Eng. J. 353 (2018) 482–489.
[7] S.A. Althobaiti, G.M. Nabil, M.E. Mahmoud, J. Mol. Liq. 429 (2025) 127597.
[8] M.I. Morariu, M. Nicolaescu, C. Orha, et al., Inorganics 13 (2025) 31.
[9] M. Akram, M. Muneer, M.I. Kanjal, et al., Radiat. Phys. Chem. 236 (2025) 112943.
[10] M.A. Abbasi, K.M. Amin, M. Ali, et al., J. Environ. Chem. Eng. 10 (2022) 107078.
[11] Q. Zhang, D. Zheng, B. Bai, et al., Chem. Eng. J. 500 (2024) 157134.
[12] R. Dulyasucharit, L. Saikhao, S. Preecharram, et al., OpenNano 24 (2025) 100249.
[13] L.V. Bora, R.K. Mewada, Sust. Energy Rev. 76 (2017) 1393–1421.
[14] L. Zhang, Y. Li, Q. Li, et al., Chem. Eng. J. 419 (2021) 129484.
[15] E.H.C. Lacerda, S.T. Medeiros, M.E.S.R. de Souza, et al., Surf. Interfaces 71 (2025) 106890.
[16] M. Tanveer, M.A. Qadeer, A.R. Ali, et al., J. Taiwan Inst. Chem. E. 169 (2025) 105976.
[17] Z. Han, Y. Lu, Y. Li, J. Alloy. Compd. 1028 (2025) 180596.
[18] S. Yasmeen, A.R. Ali, M. Tanveer, et al., Int. J. Hydrog. Energy 186 (2025) 151776.
[19] I. Ahmad, A. Al-Qattan, M.Z. Iqbal, et al., Adv. Colloid Interface Sci. 324 (2024) 103093.
[20] K. Pandi, S. Sivaperuman, J. Photoch. Photobio. A 450 (2024) 115463.
[21] C.L. Ücker, F. Riemke, V. Goetzke, et al., Chem. Phys. Impact. 4 (2022) 100079.
[22] J. Yao, F. Gao, Y. Zhao, et al., J. Colloid Interface Sci. 697 (2025) 137938.
[23] P.N. Birla, S.S. Arbuj, R. Chauhan, et al., Int. J. Hydrog. Energy 172 (2025) 151210.
[24] L.S. de Andrade, J.V. Docílio Pereira, T.S. Brasil, et al., ACS Omega 11 (2026) 5421–5435.
[25] P. Zhang, C. Peng, H. Li, et al., Sep. Purif. Technol. 286 (2022) 120406.
[26] Y. Peng, C. Lin, M. Tang, et al., Appl. Surf. Sci. 509 (2020) 145376.
[27] C.L. Ücker, R.D.G. Cantoneiro, S.R. Almeida, et al., Ceram. Int. 51 (2025) 40941–40951.
[28] X. Li, S. Yang, L. Li, et al., J. Energy Storage. 141 (2026) 119576.
[29] D. Liu, J. Wang, J. Zhou, et al., Chem. Eng. J. 369 (2019) 968–978.
[30] S. Song, J. Tu, Z. He, et al., Appl. Catal. A: Gen. 378 (2010) 169–174.
[31] F. Li, G. Liu, F. Liu, et al., J. Hazard. Mater. 452 (2023) 131237.
[32] Y. Zhang, T. Song, X. Zhou, et al., Appl. Catal. B: Environ. 316 (2022) 121622.
[33] Y. Wang, X. Hu, H. Song, et al., Appl. Catal. B: Environ. 299 (2021) 120677.
[34] D. Liu, M. Chen, T. Niu, et al., Chem. Eng. J. 493 (2024) 152625.
[35] D. Liu, J. Zhou, J. Wang, et al., Chem. Eng. J. 344 (2018) 332–341.
[36] J. Liqiang, F. Honggang, W. Baiqi, et al., Appl. Catal. B: Environ. 62 (2006) 282–291.
[37] S. Karimzadeh, S. Khameneh Asl, M. Abbasnejad, et al., Model. Simul. Mater. Sc. 33 (2025) 045002.
[38] Z. Yao, W. Yao, Y. Zhou, et al., Chin. Chem. Lett. (2025), doi:10.1016/j.cclet.2025.111977.
[39] Y. Yang, Y. Zhao, L. Yin, et al., Chem. Res. Chin. U. 41 (2025) 1067–1075.
[40] M.W. Zheng, L.T. Hoang Yen, N.T. Thuy Tran, et al., Inorg. Chem. Commun. 179 (2025) 114767.
[41] M.Z. Fidelis, Y.B. Favaro, A.S.G.G.D. Santos, et al., J. Environ. Chem. Eng. 11 (2023) 110690.
[42] C. Zhu, J. Zheng, L. Fang, et al., J. Mol. Catal. A: Chem. 424 (2016) 135–144.
[43] M. Lin, W. Qi, H. Zhang, et al., J. Photoch. Photobio. C 60-61 (2024) 100679.
[44] R.E. Núñez-Salas, A. Hernández-Ramírez, L. Hinojosa-Reyes, et al., Catal. Today 328 (2019) 202–209.
[45] J. An, X. Zhao, Y. Zhang, et al., Adv. Funct. Mater. 32 (2022) 2110119.
[46] E. Lee, A. VahidMohammadi, Y.S. Yoon, et al., ACS Sens. 4 (2019) 1603–1611.
[47] Q. Yan, G.F. Huang, D.F. Li, et al., J. Mater. Sci. Technol. 34 (2018) 2515–2520.
[48] X. Gou, B. Jiang, T. Zhu, et al., Fuel 375 (2024) 132580.
[49] Z. Liu, X. Cui, X. Yang, et al., J. Power Sources. 630 (2025) 236118.
[50] X. Wang, G. Chen, C. Zhou, et al., Eur. J. Inorg. Chem. 2012 (2012) 1742–1749.
[51] J.X. Zhao, D. Yao, L. Li, et al., Appl. Catal. A: Gen. 678 (2024) 119726.
[52] T. Yang, Z. Yang, X. Cheng, et al., J. Alloy. Compd. 876 (2021) 160145.
[53] O.F. Lopes, E.C. Paris, C. Ribeiro, Appl. Catal. B: Environ. 144 (2014) 800–808.
[54] A.L.A. Faria, H.A. Centurion, J.A. Torres, et al., J. CO_2 Util. 53 (2021) 101739.
[55] J. Gao, F. Zhang, H. Xue, et al., Appl. Catal. B: Environ. 281 (2021) 119509.
[56] T. Zhang, B. Liu, Q. Li, et al., Sep. Purif. Technol. 353 (2025) 128386.
[57] C. Li, J. Liu, H. Li, et al., Nat. Commun. 13 (2022) 2357.
[58] Y. Shi, J. Li, C. Mao, et al., Nat. Commun. 12 (2021) 5923.
[59] C. Zhang, Y. Wang, W. Sun, et al., Adv. Mater. 37 (2025) 2410632.
[60] Y. Liu, D.A. Cullen, T. Lian, J. Am. Chem. Soc. 143 (2021) 20264–20273.
[61] X. Xu, L. Meng, J. Zhang, et al., Angew. Chem. Int. Ed. 63 (2024) e202308597.
[62] C. Bie, B. Zhu, L. Wang, et al., Angew. Chem. Int. Ed. 61 (2022) e202212045.
[63] H. Liu, B. Yang, G. Liao, et al., Nat. Commun. 16 (2025) 5909.
[64] R.D. Chekuri, S.R. Tirukkovalluri, South Afr. J. Chem. Eng. 24 (2017) 183–195.
[65] T. Ni, H. Zhang, Z. Yang, et al., J. Colloid Interface Sci. 625 (2022) 466–478.
[66] H. Meng, M. Liong, T. Xia, et al., ACS Nano 4 (2010) 4539–4550.
[67] S. Zhang, X. Ren, X. Zhou, et al., J. Colloid Interface Sci. 605 (2022) 766–778.
[68] J. Peng, Z. Wang, S. Wang, et al., Chem. Eng. J. 409 (2021) 128176.
[69] J.S. Murray, P. Politzer, WIREs Comput. Mol. Sci. 1 (2011) 153–163.
[70] M. Li, Y.W. Li, P.F. Yu, et al., Chem. Eng. J. 427 (2022) 130930.
[71] J. Zheng, Q. Lin, Y. Liu, et al., Chem. Eng. J. 452 (2023) 139233.
[72] Y. Zhu, G. Wei, J. Ma, et al., Chem. Eng. J. 455 (2023) 140673.
[73] H. Ma, X. Li, Z. Pan, et al., J. Membrane Sci. 661 (2022) 120924.
[74] D. Kaushik, G. Bansal, J. Pharm. Anal. 5 (2015) 285–295.
[75] B.S. Kadu, K.D. Wani, R. Kaul-Ghanekar, et al., Chem. Eng. J. 325 (2017) 715–724.
[76] H. Fu, R. Wang, Q. Xu, et al., Appl. Catal. B: Environ. 299 (2021) 120686.
[77] P. Calza, C. Medana, M. Sarro, et al., J. Chromatogr. A 1362 (2014) 135–144.
[78] K.Y. Kumar, M.K. Prashanth, O.K. Alduaij, et al., Inorg. Chem. Commun. 134 (2021) 108987.
[79] L. Sleno, V. Campagna-Slater, D.A. Volmer, Int. J. Mass Spectrom. 255-256 (2006) 130–138.